Experimental and modeling evidence of hydroxyl radical production in iron electrocoagulation as a new mechanism for contaminant transformation in bicarbonate electrolyte

Shiwei Xie [a], Chang Li [a], Peng Liao [b,*], Jingfu Wang [b], Jingan Chen [b], Ao Qian [c], Yan Zhang [a], Taoyuan Wei [a], Dong Cheng [c], Mengqi Jia [d,*]

[a] School of Urban Construction, Wuhan University of Science and Technology, Wuhan 430065, China
[b] State Key Laboratory of Environmental Geochemistry, Institute of Geochemistry, Chinese Academy of Sciences, Guiyang 550081, China
[c] State Key Lab of Biogeology and Environmental Geology, China University of Geosciences, No. 68 Jincheng Street, East Lake High-Tech Development Zone, Wuhan, Hubei 430078, China
[d] Department of Earth, Ocean and Atmospheric Sciences, The University of British Columbia, 2207 Main Mall, Vancouver, BC V6T 1Z4, Canada

ARTICLE INFO

ABSTRACT

Iron electrocoagulation is designed for sustainable high-efficiency and high-flexibility water purification applications. Recent advances reported that hydroxyl radicals (•OH)-based oxidative transformation of organic contaminants can occur in iron electrocoagulation. However, there is still a lack of mechanistic understanding the production of •OH in bicarbonate electrolyte, which presents a critical knowledge gap in the optimization of iron electrocoagulation technology towards practical application. Combined with contaminant degradation, radical quenching experiments, and spectroscopic techniques, we found that •OH was produced at rate of 16.1 $\mu M \bullet h^{-1}$ during 30-mA iron electrocoagulation in bicarbonate electrolyte through activation of O_2 by Fe(II) under pH-neutral conditions. High yield of •OH occurred at pH 8.5, likely due to high adsorbed Fe(II) that can activate O_2 to enhance •OH production. Mössbauer and X-ray photoelectron spectroscopy measurements substantiated that Fe(II)-adsorbed lepidocrocite was the dominant solid Fe(II) species at pH 8.5. A process-based kinetic modeling was developed to describe the dynamic of •OH production, Fe(II) oxidation, and contaminant degradation processes in iron electrocoagulation. Findings of this study extend the functionality of electrocoagulation from phase separation to •OH-based advanced oxidation process, which provides a new perspective for the development of electrocoagulation-based next generation sustainable water purification technology.

1. Introduction

Iron electrocoagulation has gained increasing interest in recent years for the purification of drinking water, wastewater, and groundwater with simple design and operation (Bae et al., 2022; Bicudo et al., 2021; Heffron et al., 2019b; Kim et al., 2021; Pan et al., 2017; Tian et al., 2018). Iron electrocoagulation has long been considered as a phase separation technology. Heavy metals (Cao et al., 2017), organics (Zhu et al., 2005), and colloids (Hakizimana et al., 2017) were typically found to be removed by the mechanisms of adsorption, coprecipitation, physical enmeshment, charge neutralization, and complexation. In addition, reductive transformation mechanism can also occur in iron

electrocoagulation for its effective reduction of high-valence heavy metals (e.g., Cr(VI)) and organic pollutants (Dubrawski and Mohseni, 2013; Pan et al., 2016; Patel et al., 2011).

Oxidative transformation of contaminants has also been increasingly recognized in iron electrocoagulation (Bocos et al., 2016; Delaire et al., 2016; Heffron et al., 2019a; Kim et al., 2021; Tanneru and Chellam, 2012). By controlling redox conditions (oxic vs anoxic), current, and pH, iron electrocoagulation can produce diverse conditions of aqueous Fe(II) and a suite of Fe(II)-containing solids (Dubrawski et al., 2015). Such species of Fe(II) are important players in reactive oxidizing species (ROS, e.g., $\bullet O_2^-$, H_2O_2, •OH, and Fe(IV)-O) formation under ambient conditions (eqs 1–4) (Bataineh et al., 2012; Fang et al., 2013; Li et al.,

2021; Qian et al., 2019).

$$Fe(II) + O_2 \rightarrow Fe(III) + \bullet O_2^- \tag{1}$$

$$Fe(II) + \bullet O_2^- + 2H^+ \rightarrow Fe(III) + H_2O_2 \tag{2}$$

$$Fe(II) + H_2O_2 \rightarrow Fe(III) + \bullet OH + OH^- \tag{3}$$

$$Fe(II) + H_2O_2 \rightarrow Fe(IV) - O + H_2O \tag{4}$$
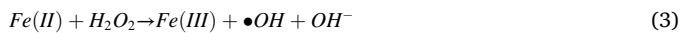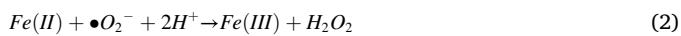
While the advanced oxidation phenomena have been reported in iron electrocoagulation, there is still a lack of mechanistic undserstanding the production of reactive oxidizing species, particularly $\bullet OH$, in the context of environmental application. Previous studies applying iron electro-coagulation have mainly focused on the demonstration of the effect of operational variables on contaminant removal performance and the production of solid products (Baran et al., 2018; Govindan et al., 2020; Maher et al., 2019), and these have not attempted to explore the kinetics and mechanims of $\bullet OH$ production. Although our recent work provided substantial knowledge on the oxidizing capacity of an iron electro-coagulation system for organic contaminant transformation, these studies were conducted using simple sulfate and chloride-based electrolyte solutions (Qian et al., 2019). To our knowledge iron electro-coagulation had not previously been revealed for $\bullet OH$ production in electrolyte composition containing bicarbonate. Bicarbonate is a major anion of groundwater in many locations around the world (Aghazadeh and Mogaddam, 2010; Gan et al., 2014; Sappa et al., 2014; Stamatis et al., 2006; Sun and Liu, 2010). In addition, bicarbonate has a significant impact on the interaction of Fe(II) and O_2 (King, 1998). As expected, the Fe(II)-O_2 reactions in iron electrocoagulation play a pivotal role in the formation of $\bullet OH$ as their interaction is a prerequisite for $\bullet OH$ production (eqs 1–4). It is foreseeable that the presence of bicarbonate could alter Fe(II) speciation and subsequent Fe(II) oxidation and molecular oxygen activation, affecting the yield of $\bullet OH$ production and contaminant transformation.

Understanding the dynamics of $\bullet OH$ and Fe speciation using direct measurements alone is challenging due to rapid rates of $\bullet OH$ and Fe(II) oxidation under ambient conditions. Dynamic simulation model is a quantitative tool for integrating complex data sets and providing their quantitative interpretations in a reaction-based framework (Pham and Waite, 2008; Steefel et al., 2005). Previous studies developed a highly constrained dynamic model that could identify As(III) oxidation and removal mechanism in iron electrocoagulation across a range of operating conditions (Delaire et al., 2017; Li et al., 2012). Our recent work established a kinetic model in an iron electrocoagulation system to predict Fe(II) oxidation and $\bullet OH$ production under various experimental conditions (Qian et al., 2019). However, these models either consider solely dissolved Fe(II) contributing to $\bullet OH$ production or lack the state-of-the-art formalisms to cope with contaminant transformation.

Building on our recent works (Qian et al., 2019; Zhang et al., 2019), the objective of this study was to fundamentally investigate the production mechanism of $\bullet OH$ in iron electrocoagulation systems in bicarbonate electrolyte. In pursuit of this objective, we first examined the oxidative transformation of a probe pollutant (i.e., aniline) and quantified the $\bullet OH$ using benzoate as a probe. We then used a combination of wet chemistry and spectroscopic techniques to identify the reaction intermediates and Fe species generated in iron electrocoagulation at different pH. We ultimately developed a process-based kinetic modeling to describe $\bullet OH$ production, Fe(II) oxidation, and contaminant degradation processes in iron electrocoagulation. Knowledge gained from this study provided important insights into the $\bullet OH$ production in iron electrocoagulation, which is critical for predicting contaminant transformation when applying for water purification.

2. Experimental methods

2.1. Chemicals

Aniline (99.5%), 2,2-bipyridine (BPY, 99.5%), N,N-diethyl-*p*-phenylenediamine (DPD), benzidine, and *p*-benzoquinone were purchased from Sinopharm Chemical Reagent Co., Ltd, China. Sodium benzoate (99.5%), *p*-aminophenol (98%), and *p*-hydroxybenzoic acid (*p*-HBA, 99%) were bought from Aladdin Biochemical Technology Co., LTD (Shanghai, China). Sodium bicarbonate, ferrous sulfate, 1,10-phenanthroline, and ammonium acetate were provided by Xilong Scientific Corporation Ltd (Guangdong, China). Methane (HPLC grade) was purchased from Fisher, Inc. 5,5-dimethyl-1-pyrroline-N-oxide (DMPO), peroxidase (POD, 113 units/mg) and ferric nitrate ($\geq$98%) were obtained from Sigma-Aldrich (Shanghai, China). Superoxide dismutase (SOD, 2500–7000 U/mg) was provided by Bomei Biotechnology. All other chemicals were at least analytic reagents. Deionized (DI) water with resistivity of 18.2 M$\Omega \bullet$cm^{-1} was used for all experiments.

2.2. Batch experiments

Electrocoagulation experiments were performed in an undivided 700-mL glass cell consisted of two pieces of Fe(0) plate (1.5 $\times$ 8.0 cm^2, 99% purity) with a distance of 2.0 cm. The reactor was filled with NaHCO$_3$ electrolyte, aniline or sodium benzoate stock solutions to a total volume of 500 mL. The selection of 10 mM HCO$_3^-$ is to mimic the bicarbonate concentrations typical encountered in groundwater conditions (see Table S1). The pH range of 6.5–8.5 was chosen because it encompasses the conditions at various groundwater remediation sites. At pH 8.5, 10 mM NaHCO$_3$ was used as a buffer. At pH 6.5 and 7.5, a flow of CO$_2$ gas (99%) was bubbled through the solution to maintain the constant pH during electrocoagulation experiments. Bubbling of CO$_2$ had negligible impact on chemical equilibrium of reactions under the conditions tested (King, 1998; Li et al., 2012). Aniline (11 μM) and sodium benzoate (10 mM) were used as probes for $\bullet OH$ production. The resulting solution was vigorously mixed by a magnetic stir bar at a high speed of 1000 rpm to improve atmospheric O$_2$ influx and room temperature. All reactors were wraped in aluminum foils to exclude the photochemical reactions that might produce ROS. Prior to each experiment, the Fe(0) electrodes were cleaned mechanically and soaked in diluted acid to remove any passive film. For oxic experiments, the reactor was exposed to air through a hole of 12 mm diameter, and the electrolytes were air-equilibrated for at least 30 min before electrolysis. For anoxic experiments, N$_2$ (99.999%) was continuously and vigorously purged through the solution throughout the electrocoagulation experiments to exclude dissolved oxygen (DO). The electrocoagulation reaction was initiated by appling a constant current of 2.5 mA$\bullet$cm^{-2} to the iron electrodes using a DC power supply (GPS-2303C, Taiwan Goodwill). All experiments were operated at least in duplicate.

2.3. Chemical analysis

For each samping event, a volume of suspension was removed from the reactor and filtered immediately through a 0.22-μm nylon membrane for the quantitation of aniline and its degradation intermediates, cumulative concentration of $\bullet OH$, dissolved Fe(II), and H$_2$O$_2$. Aniline and its degradation intermediates were analyzed by a FL2200 HPLC (Fuli Instruments) equipped with an UV–Vis detector and an Shimadzu InertSustain C18 column (5 μm, 4.6 $\times$ 250 mm). The mobile phase was a mixture of methanol and water (60:40, v/v) with a flow rate of 1 mL/min and a detection wavelength of 230 nm. Benzoate was a specific probe of $\bullet OH$ since the oxidation products were *o*-, *m*- and *p*-HBA, and the concentration of *p*-HBA was proportional to the accumulative $\bullet OH$ yield by a conversion factor of 5.87 (Joo et al., 2005; Mopper and Zhou, 1990; Zhou and Mopper, 1990). The factor was confirmed to be appropriate for the iron electrocoagulation systems in our previous work

(Qian et al., 2019). The *p*-HBA concentration was measured by the HPLC with the same column at a detection limit of 0.1 μM. The mobile phase was a mixture of 0.1% trifluoroacetic acid and acetonitrile (70:30, v/v) at a flow rate of 1 mL/min and a detection wavelength of 255 nm. The production of •OH was further validated by electro spin resonance (ESR) spectrophotometer (JOEL JES-FA200) at room temperature using DMPO (100 mM) as the spin trap. The ESR signal was cumulated 3 times to improve signal to noise ratio. The operating conditions were as following: magnetic field 326 ± 5.0 mT width, field modulation 0.1 mT, sweep time 30 s, microwave frequency 9141 MHz. H_2O_2 was detected by a modified N,N-diethyl-p-phenylenediamine (DPD) method at 551 nm, where Fe(II) was screened by 2,2-bipyridine and Fe(III) was complexed by EDTA (Katsoyiannis et al., 2008). The detection limit of H_2O_2 was 0.1 μM. Total Fe(II) was detected after extracting in 0.5 M HCl for 20–24 h, followed by filtration (Park and Dempsey, 2005). Dissolved and total Fe(II) were measured using a ferrozine method at a wavelength of 562 nm (Viollier et al., 2000). Adsorbed Fe(II) was obtained from the difference between total Fe(II) and dissolved Fe(II) (Park and Dempsey, 2005). DO was detected by a portable DO analyzer (Leici JPB-607A, Shanghai).

2.4. Solid characterization

Solid samples were collected from suspensions during and after electrocoagulation for X-ray powder diffraction (XRD), Transmission Electron Microscopy (TEM), X-ray photoelectron spectroscopy (XPS), and Mössbauer measurements. The suspensions were centrifugated, freeze-dried, and then stored in an anoxic glovebox filled with Ar (99.999%). XRD spectra was collected on a D8-FOCUS X-ray diffractometer with Cu Kα radiation (Bruker, German). TEM images were taken using a transmission electron microscope under 200 kV (Tecnai G2 F20). High-resolution XPS was collected on a PHI 5000 Versaprobe III spectrometer (ULVAC-PHI) equipped with a monochromatic Al Kα source using a pass energy of 58.7 eV. The binding energy was calibrated using the adventitious carbon C 1 s XPS peak at 284.8 eV. Mössbauer spectra were collected at 15 K using a conventional spectrometer (Germany, Wissel MS-500) equipped with a ^{57}Co(Rh) source in constant acceleration mode. The velocity was calibrated with a 7 μm α-Fe foil. Recoil software and Voigt-based models were used for the spectra fitting.

2.5. Modeling approach

Numerical modeling was performed using MIN3P, a process-based reactive transport code capable of coupling advective-diffusive flow, homogeneous and heterogeneous biogeochemical reactions (Mayer et al., 2002). The code has been used extensively in chemical species transformations, including the investigation of Fe(II)-O_2 systems associated with contaminant degradation processes (Jeen et al., 2007; Masue-Slowey et al., 2011). Additional details of numerical implement can be found in the Section I of the Supplementary Materials (SM).

The complex chemical processes operating within our experiments are translated into a chemical reaction network constrained within a set of kinetic and equilibrium parameters (Table S2). Reaction #1 describes the Fe(II) dosing from Fe anode by Faraday's law, consistent with previous modeling studies (Qian et al., 2019). Reactions #2–4 represent dissolved Fe(II) oxidations following the Haber-Weiss mechanism (Haber and Weiss, 1932). Although different Fe precipitates coexist, only FeOOH is considered to set as main Fe precipitate due to limited quantitative information on Fe precipitates, with Reactions #6–7 referring to previous model studies (Kinsela et al., 2016; Qian et al., 2019). Adsorbed Fe(II) ("Fe^{2+}-FeOOH") oxidation is included due to adsorption on FeOOH (Reaction #8), and its oxidation is assumed to follow the same pattern as dissolved Fe(II) oxidation (Reactions #9–12) (Kinsela et al., 2016). Reaction #13 represents aniline ($C_6H_5NH_2$) degradation to *p*-benzoquinone (C_6H_7NO). Finally, benzoate oxidation to HBA (Reaction #14) is included. In accordance with the conceptual model, 16 aqueous components are required to describe the relevant

chemical reactions: H^+, Na^+, CO_3^{2-}, Fe^{2+}, Fe^{3+}, $O_2(aq)$, •O_2^-, H_2O_2, •OH, FeOOH(aq), $FeOOH_i$, Fe^{2+}-FeOOH, $C_6H_5NH_2$, C_6H_7NO, benzoate, HBA, and a mineral phase represented by FeOOH(s). On the basis of the WATEQ4F (Ball and Nordstrom, 1991) and MINTEQA2 (Allison et al., 1991) databases, 18 additional aqueous complexes are identified and included in the model. Additionally, equilibrium partitioning of O_2 and CO_2 between the gas phase and the aqueous phase is considered in the model.

The chemical reactions (reactions 1–14, Table S2) are partially or fully limited by the availability of substrates, terminal electron acceptors, and inhibitors. The traditional linear rate formulation does not adequately describe the non-linear effects of chemical species (e.g., contamination degradation) (Rittmann and McCarty, 2012). In this context, a multiple Monod kinetic expression (eq. (5)) is used to describe the rate of chemical species transformations in the reaction network:

$$R_k = -k_k \prod_{j=1;o_{k,j}\neq0}^{N_c} \left(C_j^T\right)^{o_{k,j}} \prod_{j=1;K_{kj}^{in}>0}^{N_c} \frac{K_{kj}^{in}}{K_{kj}^{in}+C_j^T}\left[1-\frac{IAP_k}{K_k}\right],\ j=1,N_c \quad (5)$$

where R_k [mol $L^{-1} s^{-1}$] is the rate of kth reaction, C_j^T [mol L^{-1}] is the total concentration for component j. The total concentration terms can be envisioned as mass balance equations for the components and they implicitly include all equilibrium reactions (i.e.: $C_j^T = C_j^c + \sum_{i=1}^{N_x} v_{ij}^x C_j^x$, $j=1,N_c$; C_j^c [mol L^{-1}] and C_i^x [mol L^{-1}] are the concentration of the components j as species in solution and aqueous complex i, respectively, and v_{ij}^x defines the stoichiometric coefficient). $o_{k,j}$ defines the reaction orders with respect to the total concentration. K_{kj}^{in} is the inhibition constant [mol L^{-1}]. IAP_k defines the ion activity product and K_k is the equilibrium constant for solid phase dissolution and precipitation. In general, all kinetic parameters were based on previous studies, but in some cases were calibrated to achieve the observed chemical evolution during the batch experiments (Table S2). The changes in the chemical species can be described using the following mass balance equation:

$$\frac{dC_j^T}{dt} = \sum_{k=1}^{N_{kin}} v_{kj}R_k,\ j=1,N_c \quad (6)$$

where $v_{i,j}$ is the stoichiometric coefficient of species j in reaction k. A set of mass balance equations for chemical species are listed in Table S3. On the other hand, the equilibrium reactions for aqueous complexation and gas dissolution-exsolution can be described by the law of mass action and are provided in the Section II and IV of SM. Additionally, all equilibrium reactions and associated thermodynamic data for aqueous components, aqueous complexes, equilibrium gas partitioning with water are provided in the Section III (Tables S4–S5) and Section IV (Tables S6) of SM.

All simulation cases are summarized in the Table S7. The initial conditions used for the experiments were used for model simulations (Table S8). Model kinetic parameters were either directly constrained by previous literature, whenever available, or calibrated using a trial-and-error approach. Detailed explanation of calibrated parameters was provided in Table S2. Finally, the input and database files, as well as the selected output files for kinetic modeling, are provided as files as part of the SM.

3. Results and discussion

3.1. Identification of hydroxyl radical production in bicarbonate electrolyte

We first investigated the production of •OH by evaluating the oxidative transformation of a refractory organic contaminant, aniline, by electrocoagulation under the conditions of 10 mM $NaHCO_3$ and pH 8.5. Note that the electrolysis was performed during the entire 240 min at 2.5 mA•cm^{-2} (Fig. 1a). We found that 39 ± 1% of aniline was
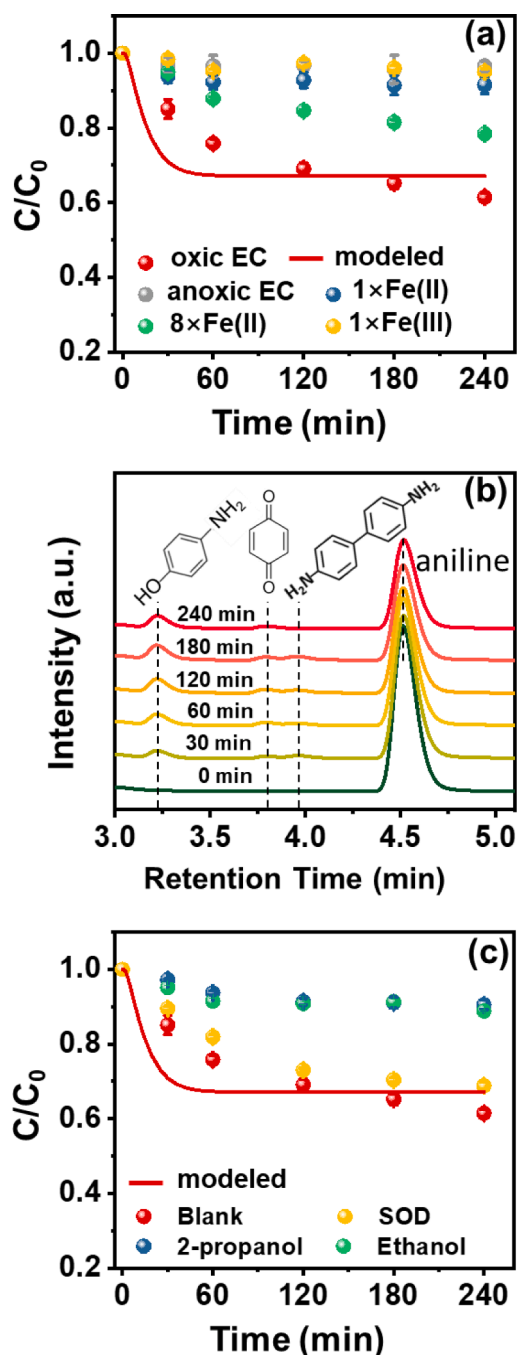
Fig. 1. (a) Time course results of the proportion of aqueous aniline remaining in the reactor during oxic electrocoagulation (EC), anoxic EC, 250 mg/L Fe(II) as $FeSO_4$ dosing by one time or 8 times, and 250 mg/L Fe(III) coagulation, respectively. (b) Multiple HPLC peaks during the oxic EC, where three products were identified to be p-aminophenol, p-benzoquinone, and benzidine. (c) Quenching experiments with SOD (25–70 U/mL), ethanol or 2-propanol (both 100 mM) during the oxic EC. Experimental conditions unless specified: pH = 8.5, [$NaHCO_3$] = 10 mM, [aniline]$_0$ = 11 μM, and I = 2.5 mA•cm^{-2} during the 240-min iron electrocoagulation.

removed in an oxic electrocoagulation system within 240 min (Fig. 1a). During the oxic electrocoagulation, O_2 from air dissolves spontaneously into the solution that could oxidize Fe(II) generated from the anode. DO rapidly dropped from initial 8.5 ± 0.2 mg/L to 4.7 ± 0.2 mg/L within 30 min and then remained stable for the remainder of the experiment (Fig. S2). This indicates an equilibrium achieved between the atmospheric O_2 influx and consumption of Fe(II) oxidation. In contrast, an

insignificant abatement (<5%) of aniline was obtained in the anoxic electrocoagulation, suggesting the necessity of DO for aniline abatement and insignificant adsorption on the precipitates. Control experiments indicated that coagulation using Fe(III) salts removed <5% of aniline (Fig. 1a), further ruling out the significant contribution of adsorption and co-precipitation mechanisms to aniline removal. However, the removal percentage of aniline was 8% by Fe(II) dosing, and further improved to 22% as the addition divided by 8 times (Fig. 1a). At pH 8.5, the rate of Fe(II) oxidation by dissolved oxygen was fast with half-lives on the order of few minutes. These results indicated that the reaction of Fe(II) with molecular oxygen might be important for aniline removal and that the multiple additions of Fe(II) improved the efficiency. HPLC analysis suggested more peaks appeared for the aniline degradation samples during electrocoagulation compared to initial aniline solution (Fig. 1b). A careful inspection of the retention times with standard compounds indicated the formation of p-aminophenol, p-benzoquinone, and benzidine (Fig. 1b). The formation of these degradation intermediates could be recognized as an evidence of •OH attacking (Brillas et al., 1998).

To clarify the nature of reactive oxidants, several probe compounds were used to quench the degradation of aniline (Fig. 1c). In addition to •OH, interactions between Fe(II) and O_2 may produce an array of other reactive oxidants that include •O_2^-, H_2O_2, and Fe(IV)-O (Keenan and Sedlak, 2008). Quenching experiments have been extensively utilized to distinguish the species of dominant reactive oxidants during the oxidation processes (Fang et al., 2013; Keenan and Sedlak, 2008; Maher et al., 2019; Tong et al., 2014; Wang et al., 2015). SOD has been used as an •O_2^- scavenger in the electrochemical system (Kim et al., 2021; Wang et al., 2015). However, the inhibitory effect of SOD on the degradation of aniline was found to be insignificant (about 19% abatement) during the iron electrocoagulation (Fig. 1c). The addition of SOD rapidly catalyzes the dismutation of •O_2^- into H_2O_2 and O_2 (eq (7)) (McCormick and Thomason, 1978). Thus we suggest that •O_2^- may not be the main oxidant for aniline.

$$2 \bullet O_2^- + 2H^+ \xrightarrow{SOD} H_2O_2 + O_2 \qquad (7)$$

We also investigated the degradation of aniline in electrocoagulation by employing excess 2-propanol and ethanol. Previous studies suggested that 2-propanol can be regarded as a selective probe for •OH, while ethanol reacts with •OH and Fe(IV)-O to form acetaldehyde (Keenan and Sedlak, 2008). Aniline degradation decreased from 39% to 9% in the presence of both ethanol and 2-propanol (Fig. 1c), suggesting that the main oxidant for aniline was presumably to be •OH. Compared to •OH, Fe(IV)-O is a weaker oxidant, as indicated by the lower oxidizing ability (standard reduction potential for Fe(IV)-O/Fe(III)= ~2.0 V/SHE versus •OH/H_2O= 2.8 V/SHE) and lower second-order rate constant for organic compounds ($k = 8.0 \times 10^1$ to $3 \times 10^5 M^{-1} s^{-1}$ versus ~$10^9 M^{-1} s^{-1}$) (Jacobsen et al., 1998; Qian et al., 2019). While Fe(IV)-O was reported to be the key reactive species for As(III) oxidation in iron electrocoagulation (Li et al., 2012), our recent work provided compelling evidence that organic degradation was most likely induced by •OH (Qian et al., 2019).

To further confirm the •OH production, we used benzoate to quantify the dynamic of •OH produced in iron electrocoagulation. This is because oxidation of benzoic acid to p-HBA can be utilized as a probe reaction, due to its weak adsorption on Fe precipitates and slow further oxidation by •OH (Qian et al., 2019; Zhang et al., 2016). The rate of cumulative •OH concentration reached about 16.1 μM•h^{-1} at pH 8.5 (Fig. 2a), which is much higher than the values of 11.2 μM•h^{-1} at pH 7.0 in a NaCl-Na_2SO_4 electrolyte (Qian et al., 2019). Interestingly, the cumulative •OH was well correlated with the degradation of aniline (R^2=0.90, Fig. 2b), corroborating the domination of •OH for aniline degradation. As a complement to •OH measurements, ESR/DMPO spin trapping experiments provided further evidence supporting the production of •OH during iron electrocoagulation, as the ESR spectrums
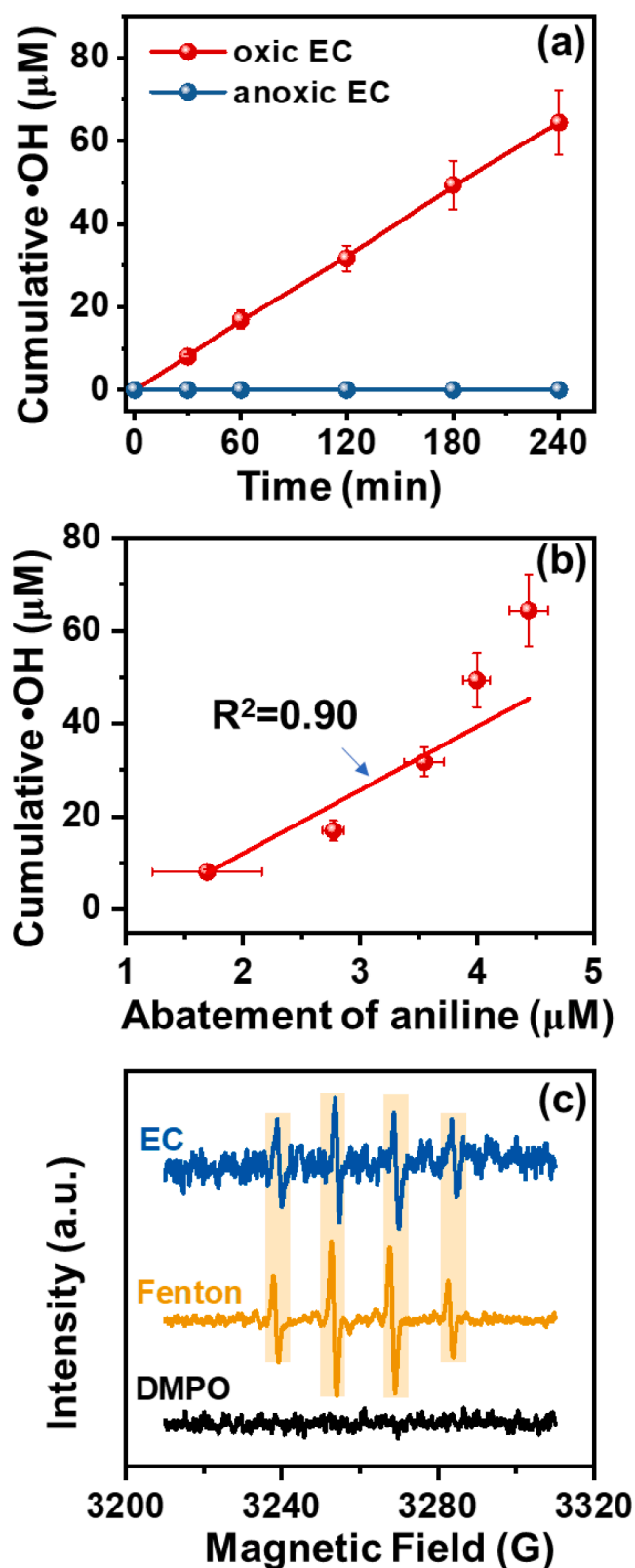
Fig. 2. (a) Cumulative •OH during the oxic electrocoagulation (EC) and anoxic EC. (b) Relationship between cumulative •OH and aniline abatement. (c) ESR spectra during the iron EC in the presence of 100 mM DMPO. Experimental conditions unless specified: pH = 8.5, [NaHCO$_3$] = 10 mM, [benzoate]$_0$ = 10 mM, and I = 2.5 mA•cm^{-2} during the 240-min iron electrocoagulation.

showed 1:2:2:1 characteristic peak of DMPO—OH (hyperfine couplings $\alpha_N = \alpha_H = 14.9$) that was in line with the spectra of the Fenton reaction (Fig. 2c).

3.2. Mechanism of hydroxyl radical production

(a) Role of H$_2$O$_2$. Theoretically, H$_2$O$_2$ may be produced through either two-electron dioxygen reduction (O$_2$ → H$_2$O$_2$) on cathode (Kim et al., 2021) or one-electron molecular oxygen activation (consecutive one-electron transfer: O$_2$ → •O^{2-} → H$_2$O$_2$) pathways (Wang et al., 2015). To distinguish the relative contribution of these pathways, the anode chamber and cathode chamber were separated by a salt bridge in a divided electrocoagulation system (Fig. S3). Results illustrated that no H$_2$O$_2$ detected in the cathode chamber, while the instantaneous H$_2$O$_2$ concentration increased to approximately 1.4 μM at 3 h in the anode chamber (Fig. 3). These observations demonstrated that one-electron molecular oxygen activation pathway was the main source of H$_2$O$_2$ during iron electrocoagulation. As one of the ROS generated from the Fe(II)-O$_2$ reactions, H$_2$O$_2$ itself could not oxidize aniline (Fig. S4) but acting as one of the key intermediates for •OH production in the iron electrocoagulation system.

(b) Effect of pH. It has been reported that the production of •OH in the reaction of Fe(II) species with O$_2$ and the subsequent organic oxidation strongly depend on solution pH (Katsoyiannis et al., 2008). We thus examined the influence of pH on aniline degradation, •OH production, and Fe(II) species. We interestingly found that the removal of aniline after 240 min reaction was increased from 19% to 24% and to 39% as the solution pH increased from 6.5 to 7.5 and to 8.5, respectively (Fig. S5). We chose the low-end (pH 6.5) and high-end (pH 8.5) conditions to explore the mechanism of •OH production. The observation of aniline oxidation was quantitatively consistent with the production of •OH, as shown in Fig. 4a, where cumulative •OH at pH 8.5 was almost double of that at pH 6.5. Similar to our observations, previous studies also found that the greater oxidation efficiency of As(III) and Mn(II) occurred at pH 8.5 compared to 6.5 during iron electrocoagulation in bicarbonate electrolytes (Li et al., 2012; van Genuchten and Pena, 2017). However, a decrease of •OH yield was reported in the homogeneous Fenton reaction as the solution pH was increased from 7.0 to 8.0 (Qian et al., 2019). These observations may reflect the different generation mechanism of reactive oxidants. The effect of bicarbonate on the Fe(II) oxidation and •OH production during iron electrocoagulation will be dissucussed later.
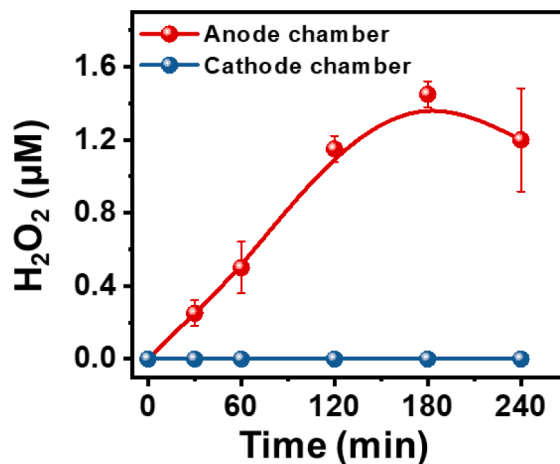

Fig. 3. Production of H$_2$O$_2$ in anode and cathode chamber during the divided electrocoagulation tests. Two cells containing 500 mL NaHCO$_3$ (10 mM) were used as the anode chamber and cathode chamber, which connected by a salt bridge prepared by 2% agar in saturated K$_2$SO$_4$. A constant current of 2.5 mA•cm^{-2} was applied during the test. The pH was controlled at 8.5 in both chambers.
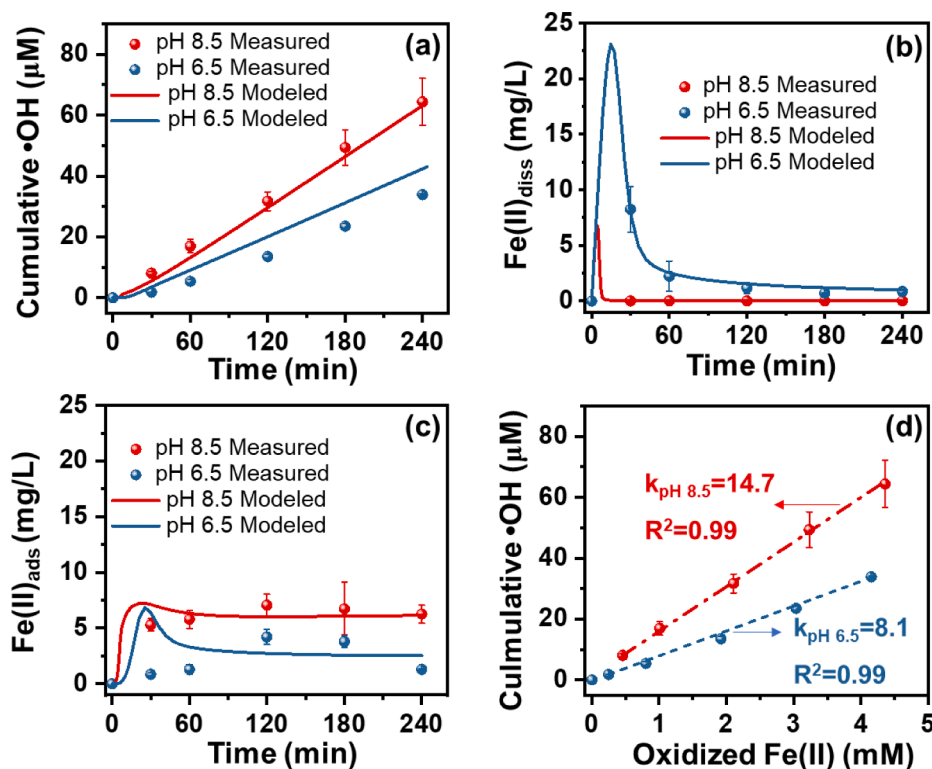
Fig. 4. (a) Cumulative •OH, variations of (b) dissolved Fe(II) (Fe(II)$_{diss}$) and (c) adsorbed Fe(II) (Fe(II)$_{ads}$), and (d) relationship between cumulative •OH and oxidized Fe(II) at pH 6.5 and 8.5 during the iron electrocoagulation process. Experimental conditions: [BA]$_0$ = 10 mM, [NaHCO$_3$] = 10 mM, and I = 2.5 mA•cm^{-2} during the 240-min iron electrocoagulation. pH variation during the electrolysis was controlled within 0.1 units (Fig. S6).

The dissolved Fe(II) concentration was increased to 8.3 mg/L within 30 min and then gradually decreased to 0.8 mg/L at pH 6.5, whereas essentially no Fe remained as dissolved Fe(II) (detection limit <0.03 mg/L) for all samples at pH 8.5 (Fig. 4b). In stark contrast, the adsorbed Fe(II) at pH 8.5 inceased to 5.3–7.1 mg/L after 30 min, almost double of that at pH 6.5 (Fig. 4c). During the iron electrocoagulation, oxidation of Fe^{2+} produced from the iron anode led to the formation of Fe(III)-oxyhydroxides (e.g., α and γ-FeOOH). At pH 6.5, the dissolved Fe(II) accumulated initially and then decreased in the later period due to accelerated oxidation by FeOOH (Tamura et al., 1980; Tanneru and Chellam, 2012). At pH 8.5, the oxidation of Fe(II) in bicarbonate solution was fast with a half-life of about 1 min (Kim et al., 2021; King, 1998; Millero et al., 1987). The fast rate of Fe(II) adsorption on FeOOH resulted in the undetectable Fe^{2+} in the solution at pH 8.5 (Liger et al., 1999; Vikesland and Valentine, 2002). Since the oxidation rate of adsorbed Fe(II) increased with increasing FeOOH concentration (Tamura et al., 1980), the fast Fe(II) oxidation limited its accumulation on the surface of FeOOH in the later stage of the reactions.

Fig. 4d illustrated a linear correlation between the cumulative •OH and oxidized Fe(II) at both pH 6.5 and 8.5. As expected, the correlation slope at pH 6.5 (8.1 ± 0.1 μM •OH per mM Fe) was much lower than that at pH 8.5 (14.7 ± 1.8 μM •OH per mM Fe). The slope at pH 8.5 indicates the yield of 14.7 μM •OH upon oxygenation of 1 mM Fe(II). This value is higher than previous electrocoagulation systems using Na$_2$SO$_4$–NaCl as electrolyte, showing a correlation slope of 10.7 at pH 7.0 (Qian et al., 2019). Further comparison shows that the yield of •OH upon Fe(II) oxygenation reported in our study is similar to prior studies using reduced clay minerals under pH-neutral conditions (Cheng et al., 2016; Yuan et al., 2018), pointing to the critical role of Fe(II) oxidation for •OH production in the iron electrocoagulation systems.

(c) Effet of bicarbonate. To reveal the role of bicarbonate, the generation of •OH in different electrolytes (NaHCO$_3$, Na$_2$SO$_4$, NaCl) was explored (Fig. 5a). For the three electrolytes, the order of •OH

production was NaHCO$_3$ > Na$_2$SO$_4$ ≈ NaCl. The most striking result was that more than twice as high •OH production in NaHCO$_3$ compared to those in Na$_2$SO$_4$ and NaCl at pH 8.5. Consistent with the production of •OH, great promotion of aniline removal was also observed for the bicarbonate electrolyte (Fig. S7). Such high •OH production in bicarbonate may be attributed to the enhanced oxidation and surface complexation of Fe(II) by carbonate. As shown in Fig. S8a, the main specie of Fe(II) was Fe^{2+} at pH 6.5, while the dominated Fe(II) species included Fe(CO$_3$)$_{(aq)}$, Fe(CO$_3$)(OH)$^-$, and Fe(CO$_3$)$_2^{2-}$ at pH 8.5. For comparison, Fe^{2+} dominated the Fe(II) species across the pH range of 6.5–8.5 for Na$_2$SO$_4$ and NaCl electrolytes (Figs. S8b-c). The rate of Fe(II) oxidation by molecular oxygen can be boosted by the complexation of carbonate, as the estimated rate constants follow k(Fe(CO$_3$)$_2^{2-}$) > k(Fe(CO$_3$)(OH)$^-$) > k(FeOH$^+$) > k(Fe^{2+}) (King, 1998; Pham and Waite, 2008). This notion is further supported by the low dissolved Fe^{2+} concentrations observed in bicarbonate electrolyte compared to Na$_2$SO$_4$ and NaCl electrolytes (Fig. 5b). At a high pH, Fe(II) oxidation rate was predominantly controlled by the oxidation of Fe(CO$_3$)$_2^{2-}$ and Fe(CO$_3$)(OH)$^-$ (Pham and Waite, 2008). It has been reported that the high reactivity of Fe(CO$_3$)$_2^{2-}$ facilitated the electron transfer from Fe(II) to O$_2$ (Caldeira et al., 2010; Pham and Waite, 2008). Furthermore, the carbonate species can cover a large fraction of sorption sites on FeOOH, and the coverage increased with increasing pH from 6 to 9 (Appelo et al., 2002; Villalobos and Leckie, 2001). The enrichment of carbonate decreased the surface charge of FeOOH (Evans et al., 1979), which could enhance the sorption of Fe(II) by the formation of Fe(II)-carbonate ternary complexes on FeOOH solids (Vikesland and Valentine, 2002). Thus, the formation of high reactive adsorbed Fe(II)-carbonate complexes might contribute to the high yields of •OH in bicarbonate electrolyte at pH 8.5.

(d) Characterization of iron solid species. Recent advances proposed that the adsorbed Fe(II) on FeOOH solids could be an important molecular oxygen activation pathway for •OH production (Qian et al.,
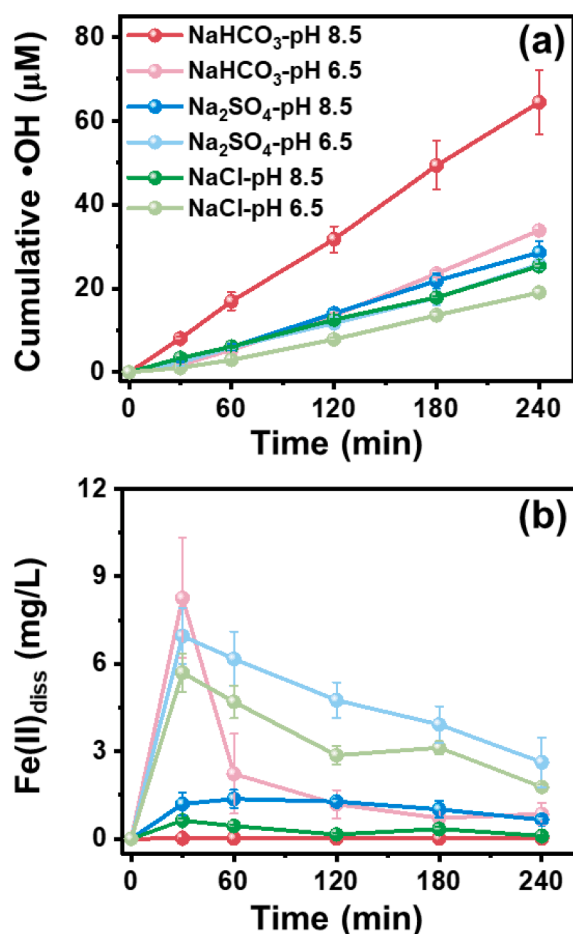
Fig. 5. (a) Cumulative •OH and (b) variations of dissolved Fe(II) (Fe(II)$_{diss}$) in different electrolyte during the iron electrocoagulation process. Please note that the data of cumulative •OH in Na$_2$SO$_4$ electrolyte at pH 6.5 was overlapped with that in NaCl electrolyte at pH 8.5. Experimental conditions unless specified: [BA]$_0$ = 10 mM, pH = 8.5 or 6.5, and I = 2.5 mA•cm^{-2} during the 240-min iron electrocoagulation.

2019). To confirm the presence of adsorbed Fe(II) in our study, the solid Fe particles formed during electrocoagulation was characterized by XRD, TEM, Mössbauer, and XPS. XRD patterns showed that the dominant iron minerals formed at pH 8.5 was lepidocrocite (Fig. S9), consistent with our previous study at comparable conditions (Pan et al., 2017). TEM images exhibited a "hedgehog-like" structure that was similar to lepidocrocite formed at pH 8.5 in bicarbonate electrolyte (Fig. S10). Mössbauer spectra collected at pH 6.5 (Fig. 6a) exhibited a prominent Fe(III) sextet consistent with goethite (Latta et al., 2012), which suggests a thorough oxidation of Fe(II) in the precipitates (Dubrawski et al., 2015; Govindan et al., 2020). For the solid samples collected at pH 8.5, however, deconvoluting the Mössbauer spectra only lead to a new Fe(III) sextet (Table S9), as reflected by center shift (CS= 0.50 mm/s), hyperfine field (H = 43.1 T), and a broad collapsed feature (CS= 0.65 mm/s, H = 29.5 T) (Fig. 6b). The Fe(III) sextet, which was comprised of 55% of the total area, could be assigned to lepidocrocite (Cheng et al., 2020), in coincidence with the XRD measurements (Fig. S9). Comparison of the collapsed feature parameter (CS= 0.65 mm/s) with previous reports in the reference (Notini et al., 2018) suggested that the collapsed feature was possibly due to the presence of adsorbed Fe(II).

To gain further insights into the surface Fe(II) species, XPS was used to indentify the iron oxides generated during the iron electrocoagulation at pH 6.5 and 8.5. As shown in Fig. 6c and Fig. S11, the Fe 2p$_{3/2}$ spectra of pH 8.5 and pH 6.5 both had a board peak near 711.0 eV, suggesting

mainly surface Fe(III) species (Qiu et al., 2017). Based on the results of Mössbauer spectra, surface Fe(III) species were fitted by goethite (α-FeOOH) and lepidocrocite (γ-FeOOH) with multiple peak structures in the Fe 2p$_{3/2}$ spectra of pH 8.5 and pH 6.5, respectively (Biesinger et al., 2011). In addition, two peaks at 708.3 eV and 709.3 eV (full wide at half maximum (FWHM) value of both 1.2 eV) were figured out in the Fe 2p$_{3/2}$ spectra, which could be assigned to a Fe(II)-O specie (Grosvenor et al., 2004; McIntyre and Zetaruk, 1977). The O 1 s spectra collected at pH 8.5 was fitted well by two peaks at 530.0 eV and 531.5 eV (Fig. 6d), ascribed to lattice oxygen binding with Fe (Fe-O) and O—H bonding, respectively (Ai et al., 2013; McIntyre and Zetaruk, 1977). The content of Fe(II)-O specie from the 60 min sample collected at pH 8.5 (9.1%) was almost double of that at pH 6.5 (4.7%) in Fe 2p$_{3/2}$ spectra (Table S10). Similarly, much higher precentage of Fe-O specie was observed for sample collected at pH 8.5 in O 1 s spectra (Tables S11). The C 1 s spectra showed a higher peak at 288.9 eV for sample collected at pH 8.5 compared to pH 6.5 (Fig. S12), suggesting a higher content of -CO$_3$ species on the surface (Heuer and Stubbins, 1999). These observations corroborated the surface complexation of Fe(II) and carbonate on FeOOH. Taken together, both Mössbauer and XPS measurements provided direct evidence for the dominant of adsorbed Fe(II) at pH 8.5 during the iron electrocoagulation process. We expected that the activation of O$_2$ by Fe(II) adsorbed on FeOOH may be a pivotal mechanism responsible for •OH production in the iron electrocoagulation systems, which is supported by our recent work showing that lepidocrocite-sorbed Fe(II) particles dominated •OH production using NaCl-Na$_2$SO$_4$ electrolytes in iron electrocoagulation (Qian et al., 2019).

3.3. Process-based kinetic modeling

According to the above mechanisms uncovered for •OH production, a process-based kinetic modeling was further used to provide additional insights into the dynamic processes affecting chemical species transformation. First, the kinetic model was evaluated for the dynamics of Fe (II) oxidation and •OH production in iron electrocoagulation. Simulation results were overall matched with the observed results for •OH, dissolved Fe(II), and adsorbed Fe(II) at pH 6.5 and 8.5 (Figs. 4a-c). Among the reaction networks, the steps for one-electron transfer to yield superoxide (Reactions #2 and #9 in Table S2) were identified as the rate-limiting step (Pham and Waite, 2008; Qian et al., 2019), so the rate constants (k$_2$ and k$_9$) were the slowest. The k$_2$ (0.25 $M^{-1}s^{-1}$) was higher than the value reported in sulfate and chloride system (Qian et al., 2019), which further suggests the acceleration of Fe(II) oxidation in the presence of bicarbonate. In addition, the rate constants of k$_2$, k$_3$, k$_4$, k$_5$, k$_9$, k$_{10}$, k$_{11}$, and k$_{12}$ were higher at pH 8.5 than that at pH 6.5, which is consistent with the high oxidation rate of Fe(II) observed at high pH.

To further investigate the relative contributions of dissolved Fe(II) and adsorbed Fe(II) to •OH and other possible reactive oxidants (i.e.: H$_2$O$_2$ and •O$_2^-$) production at different pH conditions, a system mass balance was performed. Simulation results showed that adsorbed Fe(II) was the predominant contributor to reactive oxidants production at different pH conditions. At pH 6.5 and 8.5, the adsorbed Fe(II) contributed 82.7% and 87.4% of •OH production, respectively, while the dissolved Fe(II) contributed slightly (Fig. S13). Additionally, adsorbed Fe(II) at pH 8.5 contributed to •OH production more than that at pH 6.5. These results also suggest that adsorbed Fe(II) oxidation was predominant at a high pH with progressive adsorbed Fe(II) generation in iron electrocoagulation. Taken together, model simulations confirmed that •OH can be produced through Fe(II) oxygenation, which is consistent with experimental observations that adsorbed Fe(II) oxidation contributed to •OH production under conditions tested.

The developed kinetic model also provides insight into aniline degradation. As the first step, we performed a simulation of aniline degradation that did not consider a competitive effect of bicarbonate. The model failed to capture the aniline concentrations over the entire simulation period (data not shown). Alternatively, we considered a new
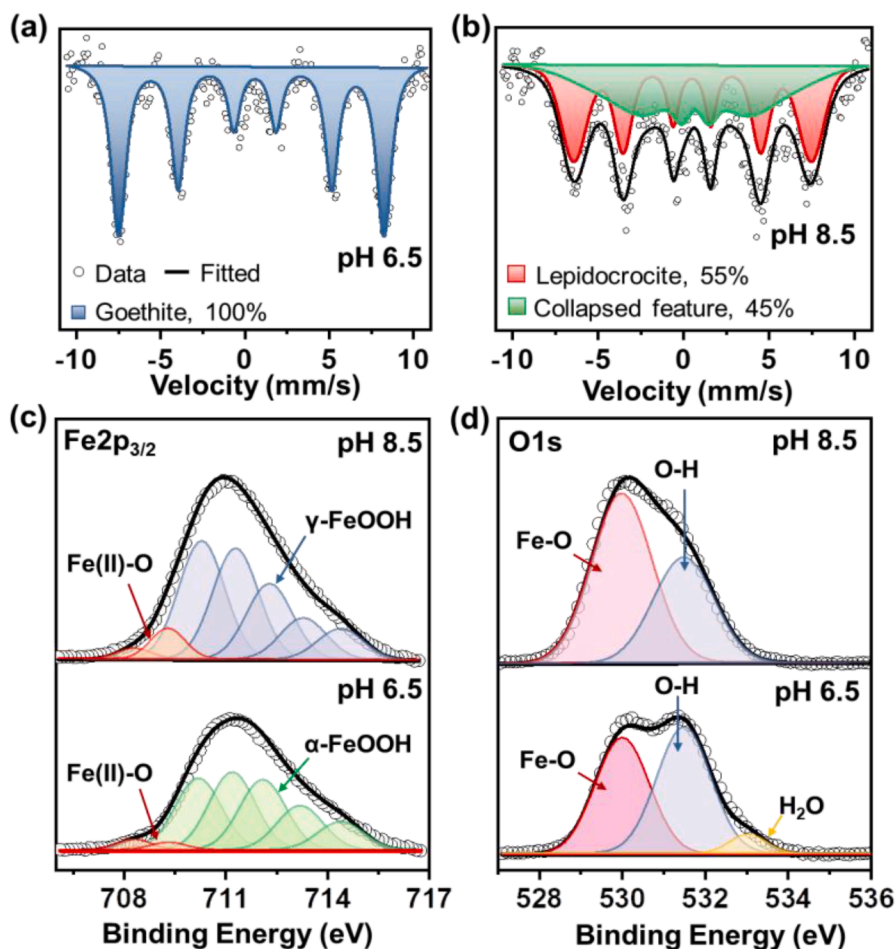
Fig. 6. Mössbauer spectra at 15 K for the Fe precipitates collected at (a) pH 6.5 and (b) pH 8.5 after 60 min electrolysis during iron electrocoagulation. Fitting and calculated Mössbauer parameters were presented in Table S9. High resolution XPS spectra of (c) Fe $2p_{3/2}$ and (d) O 1 s for Fe precipitates collected at pH 6.5 and pH 8.5 after 60 min electrolysis during iron electrocoagulation. The percentages of Fe and O species were illustrated in Tables S10 and S11.

degradation formulation by adding a CO_3^{2-} competition term into the rate expression of aniline (equation 8 in Table S3). Fig. 1a clearly shows a good agreement between the observed and simulated results for aniline degradation, suggesting the improvement of the model's capability to simulate the observed aniline concentrations. Although high concentration of bicarbonate competes with contaminants for the •OH, our observation also showed promotion of •OH production by bicarbonate. The combination effect still enabled the treatment efficiency in bicarbonate electrolyte higher than other systems (Fig. S7). We acknowledge that the introduction of a CO_3^{2-} competition term may not adequately describe the compex effect of bicarbonate. Future modeling studies could address additional complexity by considering a more detailed chemical reaction network and identifying controlling effects (i.e., promotion and competition effects).

4. Conclusion

This study to our knowledge is the first to provide new mechanism evidence for the presence of advanced oxidation phenomena during the treatment of organic pollutants in iron electrocoagulation using bicarbonate electrolyte. We demonstrated that organic pollutant could be oxidized by •OH generated through activation of O_2 during iron electrocoagulation in bicarbonate electrolyte at pH 6.5–8.5. High oxidizing capacity of iron electrocoagulation occurred at pH 8.5 in bicarbonate. The production of •OH in bicarbonate was much higher than that in Na_2SO_4 and NaCl at pH 8.5. Enhanced •OH production can be attributed to the enhanced oxidation and surface complexation of Fe(II) by

bicarbonate. The dynamic of •OH production, Fe(II) oxidation, and contaminant degradation processes in bicarbonate at pH 6.5 and 8.5 can be described by a process-based kinetic modeling. Both experimental and simulation results shed light on the importance of adsorbed Fe(II) on •OH production under the tested experimental conditions. Application of iron electrocoagulation system would be promising for micro-pollutants removal from groundwater with alkalescent bicarbonate (e. g., karst groundwater). The oxidizing capacity of iron electrocoagulation systems would be regulated by optimizing the operation conditions and electrode configuration. The combination of iron electrocoagulation with electro-Fenton process and renewable photovoltaic technology provides new perspective to develop effective and sustainable green methods for water treatment. We realize that the real groundwater environments are more complexed than the systems presented, more work is ongoing to extend the framework developed here to evaluate the production of •OH and subsequent oxidation of contaminants in actual groundwater environments.

Appendix A. Supplementary data

Additional information includes numerical implementation (Section I), equilibrium reactions for aqueous complexes (Section II), Chemical database for kinetic and equilibrium reactions (Section III), equilibrium reactions for gaseous phase (Section IV), Overview of simulation cases (Section V), and Initial conditions for components (Section VI), Figs. S1–S13, and Tables S1–S11.

Declaration of Competing Interest

We (all authors) declare that we have no known competing financial interests or personal relationships that could have appeared to influence the work reported in this paper.

Acknowledgments

Supplementary materials

Supplementary material associated with this article can be found, in the online version, at doi:10.1016/j.watres.2022.118662.

References

Aghazadeh, N., Mogaddam, A.A., 2010. Assessment of groundwater quality and its suitability for drinking and agricultural uses in the Oshnavieh Area, Northwest of Iran. J. Environ. Prot. 01 (01), 30–40.

Ai, Z., Gao, Z., Zhang, L., He, W., Yin, J.J., 2013. Core–shell structure dependent reactivity of Fe@Fe$_2$O$_3$ nanowires on aerobic degradation of 4-Chlorophenol. Environ. Sci. Technol. 47 (10), 5344–5352.

Allison, J., Brown, D. and Novo-Gradac, K., 1991. MINTEQA2/PRODEFA2, a geochemical assessment model for environmental systems: version 3. 0 user's manual. GA: US Environmental Protection Agency.

Appelo, C.A.J., Van Der Weiden, M.J.J., Tournassat, C., Charlet, L., 2002. Surface complexation of ferrous iron and carbonate on ferrihydrite and the mobilization of arsenic. Environ. Sci. Technol. 36 (14), 3096–3103.

Bae, Y., Crompton, N.M., Sharma, N., Yuan, Y., Catalano, J.G., Giammar, D.E., 2022. Impact of dissolved oxygen and ph on the removal of selenium from water by iron electrocoagulation. Water Res 213, 118159.

Ball, J.W. and Nordstrom, D., 1991. WATEQ4F - User's manual with revised thermodynamic data base and test cases for calculating speciation of major, trace and redox elements in natural waters. U.S.Geological Survey Open-File Report 91–183, 1–189.

Baran, W., Adamek, E., Jajko, M., Sobczak, A., 2018. Removal of veterinary antibiotics from wastewater by electrocoagulation. Chemosphere 194, 381–389.

Bataineh, H., Pestovsky, O., Bakac, A., 2012. pH-induced mechanistic changeover from hydroxyl radicals to iron (IV) in the Fenton reaction. Chem. Sci. 3 (5), 1594–1599.

Bicudo, B., van Halem, D., Trikannad, S.A., Ferrero, G., Medema, G., 2021. Low voltage iron electrocoagulation as a tertiary treatment of municipal wastewater: removal of enteric pathogen indicators and antibiotic-resistant bacteria. Water Res 188, 116500.

Biesinger, M.C., Payne, B.P., Grosvenor, A.P., Lau, L.W.M., Gerson, A.R., Smart, R.S.C., 2011. Resolving surface chemical states in XPS analysis of first row transition metals, oxides and hydroxides: cr, Mn, Fe, Co and Ni. Appl. Surf. Sci. 257 (7), 2717–2730.

Bocos, E., Brillas, E., Sanromán, M.Á., Sirés, I., 2016. Electrocoagulation: simply a phase separation technology? The case of bronopol compared to its treatment by EAOPs. Environ. Sci. Technol. 50 (14), 7679–7686.

Brillas, E., Mur, E., Sauleda, R., Sanchez, L., Peral, J., Domènech, X., Casado, J., 1998. Aniline mineralization by AOP's: anodic oxidation, photocatalysis, electro-Fenton and photoelectro-Fenton processes. Appl. Catal. B: Environ 16 (1), 31–42.

Caldeira, C.L., Ciminelli, V.S.T., Osseo-Asare, K., 2010. The role of carbonate ions in pyrite oxidation in aqueous systems. Geochim. Cosmochim. Acta 74 (6), 1777–1789.

Cao, D., Zeng, H., Yang, B., Zhao, X., 2017. Mn assisted electrochemical generation of two-dimensional Fe-Mn layered double hydroxides for efficient Sb(V) removal. J. Hazard. Mater. 336, 33–40.

Cheng, D., Yuan, S., Liao, P., Zhang, P., 2016. Oxidizing impact induced by mackinawite (FeS) nanoparticles at oxic conditions due to production of hydroxyl radicals. Environ. Sci. Technol. 50 (21), 11646–11653.

Cheng, D., Neumann, A., Yuan, S., Liao, W., Qian, A., 2020. Oxidative degradation of organic contaminants by FeS in the presence of O$_2$. Environ. Sci. Technol. 54 (7), 4091–4101.

Delaire, C., van Genuchten, C.M., Amrose, S.E., Gadgil, A.J., 2016. Bacteria attenuation by iron electrocoagulation governed by interactions between bacterial phosphate groups and Fe(III) precipitates. Water Res 103, 74–82.

Delaire, C., Amrose, S., Zhang, M., Hake, J., Gadgil, A., 2017. How do operating conditions affect As(III) removal by iron electrocoagulation? Water Res 112, 185–194.

Dubrawski, K.L., Mohseni, M., 2013. In-situ identification of iron electrocoagulation speciation and application for natural organic matter (NOM) removal. Water Res 47 (14), 5371–5380.

Dubrawski, K.L., van Genuchten, C.M., Delaire, C., Amrose, S.E., Gadgil, A.J., Mohseni, M., 2015. Production and transformation of mixed-valent nanoparticles generated by Fe(0) electrocoagulation. Environ. Sci. Technol. 49 (4), 2171–2179.

Evans, T.D., Leal, J.R., Arnold, P.W., 1979. The interfacial electrochemistry of goethite (α-FeOOH) especially the effect of CO$_2$ contamination. J. Electroanal. Chem. Interfacial Electrochem. 105 (1), 161–167.

Fang, G.-.D., Zhou, D.-.M., Dionysiou, D.D., 2013. Superoxide mediated production of hydroxyl radicals by magnetite nanoparticles: demonstration in the degradation of 2-chlorobiphenyl. J. Hazard. Mater. 250, 68–75.

Gan, Y., Wang, Y., Duan, Y., Deng, Y., Guo, X., Ding, X., 2014. Hydrogeochemistry and arsenic contamination of groundwater in the Jianghan Plain, central. China. J. Geochem. Explor. 138, 81–93.

Govindan, K., Angelin, A., Kalpana, M., Rangarajan, M., Shankar, P., Jang, A., 2020. Electrocoagulants characteristics and application of electrocoagulation for micropollutant removal and transformation mechanism. ACS Appl. Mat. Interfaces 12 (1), 1775–1788.

Grosvenor, A.P., Kobe, B.A., Biesinger, M.C., McIntyre, N.S., 2004. Investigation of multiplet splitting of Fe 2p XPS spectra and bonding in iron compounds. Surf. Interface Anal. 36 (12), 1564–1574.

Haber, F., Weiss, J., 1932. Über die Katalyse des Hydroperoxydes. Naturwissenschaften 20 (51), 948–950.

Hakizimana, J.N., Gourich, B., Chafi, M., Stiriba, Y., Vial, C., Drogui, P., Naja, J., 2017. Electrocoagulation process in water treatment: a review of electrocoagulation modeling approaches. Desalination 404, 1–21.

Heffron, J., McDermid, B., Maher, E., McNamara, P.J., Mayer, B.K., 2019a. Mechanisms of virus mitigation and suitability of bacteriophages as surrogates in drinking water treatment by iron electrocoagulation. Water Res 163, 114877.

Heffron, J., Ryan, D.R., Mayer, B.K., 2019b. Sequential electrocoagulation-electrooxidation for virus mitigation in drinking water. Water Res 160, 435–444.

Heuer, J.K., Stubbins, J.F., 1999. An XPS characterization of FeCO$_3$ films from CO$_2$ corrosion. Corros. Sci. 41 (7), 1231–1243.

Jacobsen, F., Holcman, J., Sehested, K., 1998. Reactions of the ferryl ion with some compounds found in cloud water. Int. J. Chem. Kinet. 30 (3), 215–221.

Jeen, S.-.W., Mayer, K.U., Gillham, R.W., Blowes, D.W., 2007. Reactive transport modeling of trichloroethene treatment with declining reactivity of iron. Environ. Sci. Technol. 41 (4), 1432–1438.

Joo, S.H., Feitz, A.J., Sedlak, D.L., Waite, T.D., 2005. Quantification of the oxidizing capacity of nanoparticulate zero-valent iron. Environ. Sci. Technol. 39 (5), 1263–1268.

Katsoyiannis, I.A., Ruettimann, T., Hug, S.J., 2008. pH dependence of Fenton reagent generation and As (III) oxidation and removal by corrosion of zero valent iron in aerated water. Environ. Sci. Technol. 42 (19), 7424–7430.

Keenan, C.R., Sedlak, D.L., 2008. Factors affecting the yield of oxidants from the reaction of nanoparticulate zero-valent iron and oxygen. Environ. Sci. Technol. 42 (4), 1262–1267.

Kim, K., Narayanan, J., Sen, A., Chellam, S., 2021. Virus removal and inactivation mechanisms during iron electrocoagulation: capsid and genome damages and electro-Fenton reactions. Environ. Sci. Technol. 55 (19), 13198–13208.

King, D.W., 1998. Role of carbonate speciation on the oxidation rate of Fe (II) in aquatic systems. Environ. Sci. Technol. 32 (19), 2997–3003.

Kinsela, A.S., Jones, A.M., Bligh, M.W., Pham, A.N., Collins, R.N., Harrison, J.J., Wilsher, K.L., Payne, T.E., Waite, T.D., 2016. Influence of dissolved silicate on rates of Fe (II) oxidation. Environ. Sci. Technol. 50 (21), 11663–11671.

Latta, D.E., Bachman, J.E., Scherer, M.M., 2012. Fe electron transfer and atom exchange in goethite: influence of Al-substitution and anion sorption. Environ. Sci. Technol. 46 (19), 10614–10623.

Li, Lei, van, G., Case, M., Addy, Susan, E.A Yao, Juanjuan, Gao, Naiyun, Gadgil, Ashok, J., 2012. Modeling As(III) oxidation and removal with iron electrocoagulation in groundwater. Environ. Sci. Technol. 46 (21), 12038–12045.

Li, M., Mo, C.-.H., Luo, X., He, K.-.Y., Yan, J.-.F., Wu, Q., Yu, P.-.F., Han, W., Feng, N.-.X., Yeung, K.L., Zhou, S.-.Q., 2021. Exploring key reaction sites and deep degradation mechanism of perfluorooctane sulfonate via peroxymonosulfate activation under electrocoagulation process. Water Res 207, 117849.

Liger, E., Charlet, L., Van Cappellen, P., 1999. Surface catalysis of uranium(VI) reduction by iron(II). Geochim. Cosmochim. Acta 63 (19), 2939–2955.

Maher, E.K., O'Malley, K.N., Heffron, J., Huo, J., Wang, Y., Mayer, B.K., McNamara, P.J., 2019. Removal of estrogenic compounds via iron electrocoagulation: impact of water quality and assessment of removal mechanisms. Environ. Sci. Water Res. Technol. 5 (5), 956–966.

Masue-Slowey, Y., Kocar, B.D., Bea Jofré, S.A., Mayer, K.U., Fendorf, S., 2011. Transport implications resulting from internal redistribution of arsenic and iron within constructed soil aggregates. Environ. Sci. Technol. 45 (2), 582–588.

Mayer, K.U., Frind, E.O., Blowes, D.W., 2002. Multicomponent reactive transport modeling in variably saturated porous media using a generalized formulation for kinetically controlled reactions. Water Resour. Res. 38 (9), 13-11–13-21.

McCormick, J., Thomason, T., 1978. Near-ultraviolet photooxidation of tryptophan. Proof of formation of superoxide ion. J. Am. Chem. Soc. 100 (1), 312–313.

McIntyre, N.S., Zetaruk, D.G., 1977. X-ray photoelectron spectroscopic studies of iron oxides. Anal. Chem. 49 (11), 1521–1529.

Millero, F.J., Sotolongo, S., Izaguirre, M., 1987. The oxidation kinetics of Fe (II) in seawater. Geochim. Cosmochim. Acta 51 (4), 793–801.

Mopper, K., Zhou, X., 1990. Hydroxyl radical photoproduction in the sea and its potential impact on marine processes. Science 250 (4981), 661–664.

Notini, L., Latta, D.E., Neumann, A., Pearce, C.I., Sassi, M., N'Diaye, A.T., Rosso, K.M., Scherer, M.M., 2018. The role of defects in Fe (II)–goethite electron transfer. Environ. Sci. Technol. 52 (5), 2751–2759.

Pan, C., Troyer, L.D., Catalano, J.G., Giammar, D.E., 2016. Dynamics of chromium (VI) removal from drinking water by iron electrocoagulation. Environ. Sci. Technol. 50 (24), 13502–13510.

Pan, C., Troyer, L.D., Liao, P., Catalano, J.G., Li, W., Giammar, D.E., 2017. Effect of humic acid on the removal of chromium(VI) and the production of solids in iron electrocoagulation. Environ. Sci. Technol. 51 (11), 6308–6318.

Park, B., Dempsey, B.A., 2005. Heterogeneous oxidation of Fe(II) on ferric oxide at neutral pH and a low partial pressure of O_2. Environ. Sci. Technol. 39 (17), 6494–6500.

Patel, U.D., Ruparelia, J.P., Patel, M.U., 2011. Electrocoagulation treatment of simulated floor-wash containing Reactive Black 5 using iron sacrificial anode. J. Hazard. Mater. 197, 128–136.

Pham, A.N., Waite, T.D., 2008. Oxygenation of Fe (II) in natural waters revisited: kinetic modeling approaches, rate constant estimation and the importance of various reaction pathways. Geochim. Cosmochim. Acta 72 (15), 3616–3630.

Qian, A., Yuan, S., Xie, S., Tong, M., Zhang, P., Zheng, Y., 2019. Oxidizing capacity of iron electrocoagulation systems for refractory organic contaminant transformation. Environ. Sci. Technol. 53 (21), 12629–12638.

Qiu, G., Gao, T., Hong, J., Tan, W., Liu, F., Zheng, L., 2017. Mechanisms of arsenic-containing pyrite oxidation by aqueous arsenate under anoxic conditions. Geochim. Cosmochim. Acta 217, 306–319.

Rittmann, B.E. and McCarty, P.L., 2012. Environmental biotechnology: Principles and Applications, Tata McGraw-Hill Education.

Sappa, G., Ergul, S., Ferranti, F., 2014. Geochemical Modeling and Multivariate Statistical Evaluation of Trace Elements in Arsenic Contaminated Groundwater Systems of Viterbo Area, 3. SpringerPlus, (Central Italy), p. 237.

Stamatis, G., Lambrakis, N., Alexakis, D., Zagana, E., 2006. Groundwater quality in Mesogea basin in eastern Attica (Greece). Hydrol. Process. 20 (13), 2803–2818.

Steefel, C.I., DePaolo, D.J., Lichtner, P.C., 2005. Reactive transport modeling: an essential tool and a new research approach for the Earth sciences. Earth Planet. Sci. Lett. 240 (3), 539–558.

Sun, H., Liu, Z., 2010. Wet–dry seasonal and spatial variations in the $\delta^{13}C$ and $\delta^{18}O$ values of the modern endogenic travertine at Baishuitai, Yunnan, SW China and their paleoclimatic and paleoenvironmental implications. Geochim. Cosmochim. Acta 74 (3), 1016–1029.

Tamura, H., Kawamura, S., Hagayama, M., 1980. Acceleration of the oxidation of Fe^{2+} ions by Fe (III)-oxyhydroxides. Corros. Sci. 20 (8), 963–971.

Tanneru, C.T., Chellam, S., 2012. Mechanisms of virus control during iron electrocoagulation – Microfiltration of surface water. Water Res 46 (7), 2111–2120.

Tian, Y., He, W., Liang, D., Yang, W., Logan, B.E., Ren, N., 2018. Effective phosphate removal for advanced water treatment using low energy, migration electric–field assisted electrocoagulation. Water Res 138, 129–136.

Tong, M., Yuan, S., Zhang, P., Liao, P., Alshawabkeh, A.N., Xie, X., Wang, Y., 2014. Electrochemically induced oxidative precipitation of Fe(II) for As(III) oxidation and removal in synthetic groundwater. Environ. Sci. Technol. 48 (9), 5145–5153.

van Genuchten, C.M., Pena, J., 2017. Mn(II) oxidation in Fenton and Fenton-type systems: identification of reaction efficiency and reaction products. Environ. Sci. Technol. 51 (5), 2982–2991.

Vikesland, P.J., Valentine, R.L., 2002. Iron oxide surface-catalyzed oxidation of ferrous iron by monochloramine: Implications of oxide type and carbonate on reactivity. Environ. Sci. Technol. 36 (3), 512–519.

Villalobos, M., Leckie, J.O., 2001. Surface complexation modeling and FTIR study of carbonate adsorption to goethite. J. Colloid Interface Sci. 235 (1), 15–32.

Viollier, E., Inglett, P.W., Hunter, K., Roychoudhury, A.N., Van Cappellen, P., 2000. The ferrozine method revisited: fe(II)/Fe(III) determination in natural waters. Appl. Geochem. 15 (6), 785–790.

Wang, L., Cao, M., Ai, Z., Zhang, L., 2015. Design of a highly efficient and wide ph electro-fenton oxidation system with molecular oxygen activated by ferrous–tetrapolyphosphate complex. Environ. Sci. Technol. 49 (5), 3032–3039.

Yuan, S., Liu, X., Liao, W., Zhang, P., Wang, X., Tong, M., 2018. Mechanisms of electron transfer from structrual Fe(II) in reduced nontronite to oxygen for production of hydroxyl radicals. Geochim. Cosmochim. Acta 223, 422–436.

Zhang, P., Yuan, S., Liao, P., 2016. Mechanisms of hydroxyl radical production from abiotic oxidation of pyrite under acidic conditions. Geochim. Cosmochim. Acta 172, 444–457.

Zhang, Y., Wei, T., Fu, W., Xie, S., 2019. Hydroxyl radical induced by iron electrocoagulation for oxidative degradation of sulfonamide in groundwater. Chinese J. Environ. Eng. 13 (4), 871–877.

Zhou, X., Mopper, K., 1990. Determination of photochemically produced hydroxyl radicals in seawater and freshwater. Mar. Chem. 30, 71–88.

Zhu, B., Clifford, D.A., Chellam, S., 2005. Comparison of electrocoagulation and chemical coagulation pretreatment for enhanced virus removal using microfiltration membranes. Water Res 39 (13), 3098–3108.